

# Simple and Effective Synthesis of Indoor 3D Scenes

Jing Yu Koh<sup>\*,1</sup>, Harsh Agrawal<sup>\*,\*\*,2</sup>,  
Dhruv Batra<sup>2</sup>, Richard Tucker<sup>1</sup>, Austin Waters<sup>1</sup>, Honglak Lee<sup>3</sup>,  
Yinfei Yang<sup>\*\*,4</sup>, Jason Baldridge<sup>1</sup>, and Peter Anderson<sup>1</sup>

<sup>1</sup> Google Research

<sup>2</sup> Georgia Institute of Technology

<sup>3</sup> University of Michigan

<sup>4</sup> Apple

**Abstract.** We study the problem of synthesizing immersive 3D indoor scenes from one or more images. Our aim is to generate high-resolution images and videos from novel viewpoints, including viewpoints that extrapolate far beyond the input images while maintaining 3D consistency. Existing approaches are highly complex, with many separately trained stages and components. We propose a simple alternative: an image-to-image GAN that maps directly from reprojections of incomplete point clouds to full high-resolution RGB-D images. On the Matterport3D and RealEstate10K datasets, our approach significantly outperforms prior work when evaluated by humans, as well as on FID scores. Further, we show that our model is useful for generative data augmentation. A vision-and-language navigation (VLN) agent trained with trajectories spatially-perturbed by our model improves success rate by up to 1.5% over a state of the art baseline on the R2R benchmark. Our code will be made available to facilitate generative data augmentation and applications to downstream robotics and embodied AI tasks. Video results: <https://youtu.be/lhwwlrRfFp0>

**Keywords:** 3D scene synthesis, novel view synthesis, vision-and-language navigation

## 1 Introduction

We study the problem of synthesizing immersive 3D indoor scenes from one or more context images captured along a trajectory. Our aim is to generate high-resolution images and videos from novel viewpoints, including viewpoints that extrapolate far beyond the context image(s), while maintaining the 3D consistency of the scene. Solving this problem would make photos and videos interactive and immersive, with applications not only to content creation but also robotics and embodied AI. For example, models that can predict around

\* Equal contribution.

\*\* Work done while at Google.

corners could be used by navigation agents as world models [21] for model-based planning in novel environments [37,16]. Such models could also be used to train agents in interactive environments synthesized from static images and videos.

Previous approaches attempting this under large viewpoint changes [71,37,55] typically operate on point clouds, which are accumulated from the available context images. The use of point clouds naturally incorporates camera projective geometry into the model and helps maintain the 3D consistency of the scene [44]. To generate novel views, these approaches reproject the point-cloud relative to the target camera pose into an RGB-D *guidance image*. These guidance images are extremely sparse because of missing context and completing them requires extensive inpainting and outpainting. In prior work, Pathdreamer [37] achieves this by assuming the availability of semantic segmentations, and combining a stochastic depth and semantic segmentation (structure) generator with an RGB image generator infused with semantic, depth and guidance information via Multi-SPADE spatially adaptive normalization layers [51,44]. On the other hand, PixelSynth [55] creates guidance images using a differentiable point cloud renderer, generates a support set of additional views using PixelCNN++ [58] operating on the latent space of a VQ-VAE [53], combines and refines these images using a GAN [20] similar to SynSin [71], and then repeats this process over many samples using a combination of discriminator loss and the entropy of a scene classifier to select the best output.

We propose a simple alternative: an image-to-image GAN that maps directly from guidance images to high-resolution photorealistic RGB-D (see Fig. 1). Compared to Pathdreamer, our simple model forgoes the stochastic structure generator, spatially adaptive normalization layers, dependence on semantic segmentations, and multi-step training. By dropping the dependence of semantic segmentation inputs, we unlock training on a much broader range of data, such as more commonly available RGB-D datasets [72,39,50], and video data such as the RealEstate10K dataset [78] from YouTube. We eschew many components of PixelSynth: differentiable rendering, support set generation using PixelCNN++ and a VQ-VAE, and the multiple sampling and re-ranking procedure.

Perhaps surprisingly, with random masking of the guidance images during training, plus other architectural changes supported by thorough ablation studies, our lightweight approach outperforms prior work. In human evaluations of image quality, our model is preferred to Pathdreamer in 60% of comparisons and preferred to PixelSynth in 77%. Our FID scores on 360° panoramic images from Matterport3D [7] improve over Pathdreamer’s by 27.9% relatively (from 27.2 to 19.6) when predicting single step viewpoint changes (an average of 2.2m), and from 65.8 to 58.0 when predicting over longer trajectories containing a sequence of 6 novel viewpoints. On RealEstate10K [78] – a collection of real estate video walkthroughs from YouTube – our FID scores outperform PixelSynth, improving from 25.5 to 23.5 (and from 23.6 to 21.5 for indoor images). Our model is capable of composing compelling 3D synthetic environments from a single image, which can be used to produce realistic video renderings.<sup>5</sup>

<sup>5</sup> Video results: <https://youtu.be/lhwwlrRfFp0>

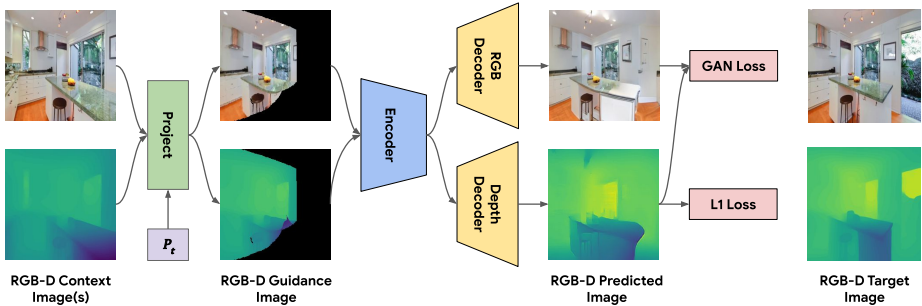


Fig. 1: Our lightweight approach to 3D scene synthesis accumulates context images in an RGB point cloud. To generate a new viewpoint, we simply apply an image-to-image GAN to the *guidance image* of the reprojected point cloud. We achieve surprisingly strong results with this simple approach, significantly outperforming more complicated models.

Motivated by these strong results on image generation, we investigate the usefulness of our model for data augmentation in embodied AI. For this purpose, we focus on the task of vision-and-language navigation (VLN) using the Room-to-Room (R2R) dataset [2], which requires an agent to follow natural language navigation instructions in previously unseen photorealistic environments. Training data for the task consists of instruction-trajectory demonstrations, where each trajectory is defined by a sequence of high-resolution 360° panoramas from the Matterport3D dataset. Inspired by trajectory augmentations with camera hardware for self-driving cars [10,6], we hypothesize that spatially perturbing the location of the captured images could reduce overfitting to the incidental details of these trajectories, and improve generalization to unseen environments. We first create an improved baseline by upgrading the VLN $\odot$ BERT agent [28] to use much stronger MURAL [31] image features (+5% success rate). We then implement synthetic trajectory augmentation by using our model to spatially perturb the location of the training panoramas by up to 1.5m while training the agent. This augmentation improves the agent’s success rate in unseen environments by an additional 1% on its own, or 1.5% when combined with renders of spatially-perturbed images from the Habitat [60] simulator – achieving state-of-the-art performance on the R2R test set (Tab. 4). In contrast, traditional image data augmentation techniques such as cropping, color distortion and blurring do not yield improvements. Our code will be made publicly available to facilitate generative trajectory augmentation and applications to downstream tasks.

## 2 Related Work

### 2.1 Novel View Synthesis

Synthesizing novel views from sets of 2D images has been studied extensively in multi-view geometry [12,4,81], and more recently with deep learning based approaches [18,35,25,17,66,79,46]. These methods use different 3D scene represen-

tations, such as point cloud representations [71], layered depth images [14], and mesh representations [63]. More recently, Neural Radiance Fields (NeRF) [47] models have gained popularity for novel view synthesis. NeRFs optimize an underlying continuous volumetric scene function, learning an implicit representation of a 3D scene from a collection of images. Follow up papers improve upon the original NeRF formulation by extending it to large-scale environments [69], unconstrained photo collections [45], learning scene priors [74], using multi-scale representations [5], reducing the amount of input images required [32], and more. Currently, NeRF models primarily focus on scene representation rather than generalization to unseen environments, and are unable to perform realistic synthesis of previously unseen 3D scenes at high resolution (which is our focus).

Whereas early work in novel view synthesis focused on smaller view changes and settings with multiple input images, recent methods tackle single-image novel view synthesis [70,29,64] and large viewpoint changes [71,37,55,56]. [54] is concurrent work with ours, which focuses on long-term future prediction for indoor scenes. The primary challenge of this task is handling both inpainting of missing pixels, and outpainting of large regions of the image from limited context, while maintaining consistency with the existing scene. The closest works to ours are PixelSynth [55] and Pathdreamer [37], which we discuss extensively in Sec. 1.

## 2.2 Point Cloud Rendering

A number of previous works explore rendering novel views from point clouds. The Gibson simulator [73] combined point cloud rendering with a neural net ‘filler’ to fix artifacts and produce more realistic images, although the neural net was trained with perceptual loss [34] rather than GAN based losses. Several papers [75,19] propose methods to inpaint object point clouds with new points in order to fill holes, which would allow more realistic images can be synthesized. [65] proposes a model which takes a colored 3D point cloud of a scene as input, and synthesizes a photo-realistic image from a novel viewpoint. [11] relies only on the semantics of a scene to synthesize a panoramic color image from a given full 3D LiDAR point cloud. These methods often consider smaller point clouds, which limits their efficiency and viability for high resolution imagery. For example, [65] trains on point clouds of size  $4096 \times 6$ , while the accumulated point cloud for our method uses RGB-D images of size  $1024 \times 512$ , and are at least  $64\times$  larger.

## 2.3 Generative Data Augmentation

Generative models propose an exciting alternative to standard data augmentation approaches. A well trained generative model can synthesize artificial samples that match the distribution and characteristics of an underlying dataset, augmenting the training set with additional novel examples [3,59]. We examine whether novel view synthesis can be used to create new training trajectories for a navigation agent, by spatially-perturbing camera viewpoints *post hoc*.

In imitation learning, expert demonstrations must be augmented to minimize the differences between the state distribution seen in training, and those induced



by the agent during inference, which otherwise causes compounding errors [57]. In practice this usually means augmenting the dataset with examples of recoveries from error, which may be rare in expert demonstrations. For example, robots and self-driving vehicles [10,6] can be instrumented to record from three cameras simultaneously (one facing forward and two shifted to the left and right). This allows recordings from the shifted cameras, as well as intermediate synthetically reprojected views, to be added to the training set with adjusted control signals to simulate recovery from drift [10,6]. In effect, we propose a flexible, hardware-free alternative to the multi-camera setup. We investigate this in the context of indoor vision-and-language navigation (VLN) on the R2R dataset [2]. To the best of our knowledge, we are the first to show benefits from data augmentation using novel view synthesis models in a photorealistic setting.

### 3 Approach

We aim to synthesize high-resolution images and videos from novel viewpoints in buildings, conditioning on one or more RGB and depth (RGB-D) observations as context. Specifically, given context consisting of a sequence of RGB-D image observations and their associated camera poses  $(I_{1:t-1}, P_{1:t-1})$ , our goal is to generate realistic RGB-D images for one or more target camera poses  $[P_t, P_{t+1}, \dots, P_T]$ . Target poses may require extrapolating far beyond the context images (e.g., predicting around corners), requiring the model to generate and in-fill potentially large regions of missing information – even entire rooms.

#### 3.1 Depth Estimation and Guidance Images

Our model requires depth values and camera poses for the context images  $(I_{1:t-1}, P_{1:t-1})$  to create an accumulated point-cloud. Given a new pose  $P_t$ , we reproject our accumulated point cloud, similar to [44,41,37] into an image from that viewpoint. We call that image a *guidance image* because it will be used to guide the inpainting and outpainting process later. In our experiments, we report results using both ground-truth and estimated depth values and camera poses, depending on the dataset. When predicting over multiple steps  $[P_t, P_{t+1}, \dots, P_T]$ , *predictions* are accumulated in the point cloud to maintain 3D consistency. We do not make assumptions about the input image format, which enables our model to run on equirectangular panoramas from Matterport3D [7] as well as perspective images from RealEstate10K [78]. To accommodate both formats, we simply use the appropriate camera models (while keeping model architecture the same).

#### 3.2 Model Architecture

We propose a simple, single-stage, end-to-end trainable model to convert a *guidance image* directly into a high-resolution photorealistic RGB-D output. Fig. 1 provides an overview of this process. Our model uses an encoder-decoder CNN architecture inspired by RedNet [33]. We use ResNet-101 [24] as the encoder, and

a ‘mirror image’ of the ResNet-101 as the decoder, replacing convolutions with transposed convolutions for upsampling. A single encoder is used for processing both the RGB and depth inputs in the guidance, but separate decoders are used for predicting RGB and depth outputs. Following RedNet, skip connections are introduced between the encoder and decoders to preserve spatial information.

Plausibly inpainting or outpainting large image regions that lack input guidance is a major challenge, e.g. when predicting around corners or under large viewpoint changes. To improve the performance of the model under these conditions, we replace all convolutions in the encoder with partial convolutions [42]. Partial convolutions only convolve valid regions in the input with the convolution kernels, so the output features are minimally affected by missing pixels in the guidance images. We also increase the effective receptive field size of the model by adding four additional convolutional layers to the output of the encoder. This allows the model to handle large regions of missing input information by propagating non-local information. We found that this was essential, and the model does not learn anything meaningful using regular convolutions.

We also experimented with the SVG [13] structure generator proposed in [37]. This module learns a prior distribution which models stochasticity in the predictions. During training, the prior distribution is learnt by minimizing KL-divergence from the posterior distribution derived from ground truth data. At inference time, different outputs can be generated by sampling from the prior distribution. In our experiments, we found that generation quality was worse when this module was included (as measured by FID and visual inspection), despite improvement in image diversity (more details in Sec. 4.2). Hence, we omit the SVG module in our final model for the sake of simplicity and performance. However, we stress that this module can be easily incorporated into our encoder to enable a trade-off between generation quality and diversity.

### 3.3 Loss Functions

The encoder-decoder model  $G$  is optimized to minimize a joint loss consisting of an  $L_1$  loss between the predicted depth  $\hat{d}_t$  and the ground-truth depth  $d_t$ , and an adversarial loss on depth and RGB images. The discriminator  $D$  used for adversarial training is based on PatchGAN [30], and applied to the 4-channel RGB-D image (either generated  $[\hat{I}_t, \hat{d}_t]$  or ground-truth  $[I_t, d_t]$ ). Note that while the use of separate decoders could allow for greater divergence between the RGB and depth predictions, this is mitigated by the discriminator which helps to enforce consistency between RGB and depth, which is essential for multi-step predictions. The training losses for the generator and discriminator are:

$$\begin{aligned}\mathcal{L}_G &= -\lambda_{\text{GAN}} \mathbb{E}_{x_t} \left[ D(G(I_{1:t-1}, T_{1:t})) \right] + \lambda_D \left\| \hat{d}_t - d_t \right\|_1 \\ \mathcal{L}_D &= -\mathbb{E}_{x_t} \left[ \min(0, -1 + D(I_t)) \right] \\ &\quad - \mathbb{E}_{x_t} \left[ \min(0, -1 - D(G(I_{1:t-1}, T_{1:t}))) \right]\end{aligned}\tag{1}$$

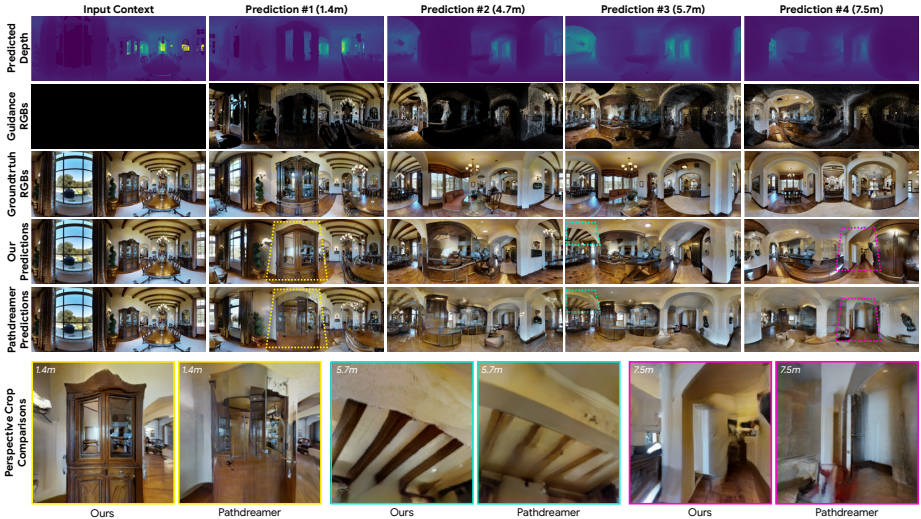


Fig. 2: Qualitative example of a prediction sequence in a previously unseen Matterport3D building. One RGB-D pano is provided as context, and a sequence of panos at novel viewpoints (up to 7.5m away) are generated. Our predictions are clearer than Pathdreamer [37], despite using a simpler model that does not require semantic segmentation inputs. Notice, in last row, our model produces more realistic images of the wooden cabinet at 1.4m, the ceiling rafters at 5.7m, and the passageway 7.5m away.

Notably, we avoid the VGG perceptual loss commonly used in prior work on conditional image synthesis [51, 37, 44] as we find that it is unnecessary for strong performance. We justify this through careful ablation experiments in Sec. 4.2.

In all experiments we train the model end-to-end from scratch, and we randomly mask up to 75% of the input guidance image for data augmentation. Masking has been shown to be an effective method of pre-training visual representations [23, 15]. We similarly find that this masking strategy significantly improves the generation quality of our model in unseen environments.

## 4 View Synthesis Experiments

We conduct experiments on two datasets of diverse indoor environments: Matterport3D [7], which contains 3D meshes of 90 buildings reconstructed from 11k high-resolution RGB-D panoramas (panos), and RealEstate10K [78], a collection of up to 10,000 YouTube video walkthroughs of real estate properties. Few prior works attempt view synthesis from a single image under large viewpoint changes. We compare to PixelSynth [55], which builds on and outperforms SynSin [71], and Pathdreamer [37]. We report automated Fréchet Inception Distance (FID) [26] scores (lower is better) and pairwise human evaluations of image quality.

Table 1: FID scores ( $\downarrow$ ) for generated RGB sequences on R2R paths in Matterport3D, using 1–3 context images. On Val-unseen, our model outperforms Pathdreamer for both 1 step and 1–6 step prediction in all settings.

Model	Context	Inputs			Val-Seen		Val-Unseen	
		Seg	RGB	Depth	1 Step	1–6 Steps	1 Step	1–6 Steps
Pathdreamer [37]	1	✓	✓	✓	26.2	41.7	34.8	70.4
Pathdreamer <sup>†</sup>	1	✓	✓	✓	20.4	<b>36.0</b>	27.2	65.8
Ours	1	-	✓	✓	<b>19.4</b>	55.4	<b>19.6</b>	<b>58.0</b>
Pathdreamer [37]	2	✓	✓	✓	25.8	38.4	38.2	61.0
Pathdreamer <sup>†</sup>	2	✓	✓	✓	19.8	<b>32.6</b>	31.4	55.8
Ours	2	-	✓	✓	<b>19.3</b>	45.3	<b>22.4</b>	<b>49.5</b>
Pathdreamer [37]	3	✓	✓	✓	25.6	36.7	38.5	52.9
Pathdreamer <sup>†</sup>	3	✓	✓	✓	19.6	<b>30.2</b>	32.0	47.1
Ours	3	-	✓	✓	<b>19.0</b>	39.0	<b>22.3</b>	<b>39.9</b>

<sup>†</sup>Restated results excluding blurred regions (directly comparable to ours).

## 4.1 Matterport3D

Both PixelSynth and Pathdreamer report results on Matterport3D. However, as concurrent works, the evaluation procedures are not comparable. PixelSynth is trained and evaluated on  $256 \times 256$  perspective renders from the reconstructed 3D meshes. These renders are not photorealistic and often contain large regions of missing/black pixels due to poor reconstruction. Pathdreamer is trained and evaluated on the high-res  $1024 \times 512$   $360^\circ$  panoramic images, and evaluated over multiple steps of prediction. Therefore, on the Matterport3D dataset we follow the more challenging Pathdreamer evaluation procedure.

*Training and Evaluation.* Following Pathdreamer, we train our model using  $1024 \times 512$  equirectangular RGB-D images and ground-truth pose information. Unlike Pathdreamer, our model does not require ground-truth semantic segmentations as input, and we train for only single-step prediction, i.e., predicting the pano at an adjacent viewpoint using one context pano as input. Evaluations are based on paths from the Val-Seen and Val-Unseen splits of the Room-to-Room (R2R) dataset [2], which are comprised of sequences of adjacent panoramas (2.2m apart on average). Given the first RGB-D pano in the path and its  $(x, y, z)$  pose as context, the model must generate panos for the remainder of the path given only their poses (up to a maximum of 6 steps).

*FID Scores.* In Tab. 1 we report FID scores for the generated RGB images over 1–6 prediction steps (representing trajectory rollouts of 2–13m), using from 1–3 panos as context. We evaluate in two settings – novel viewpoints in environments seen during training (Val-Seen) and previously unseen (Val-Unseen) environments. Since the top and bottom 12.5% of each Matterport3D pano is blurred, we crop these areas before calculating FID and re-state the previously reported results from Pathdreamer for fair comparison. On Val-Unseen, based on FID score, our model outperforms Pathdreamer in all settings. When using a single context image for 1-step prediction, we improve FID scores from

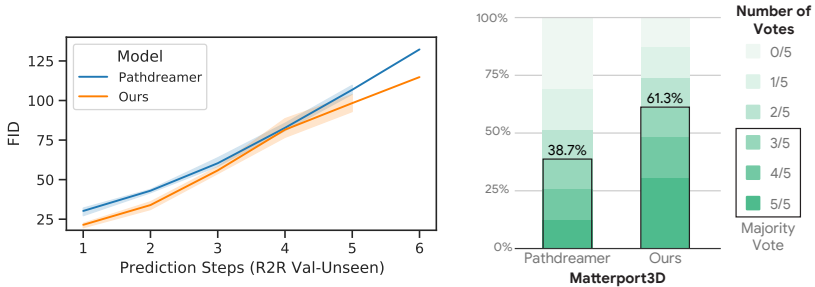


Fig. 3: FID scores ( $\downarrow$ ) over multiple steps of prediction on Matterport3D (left), and human evaluations ( $\uparrow$ ) comparing our model to Pathdreamer (right).

27.6 to 19.6. Similarly, when using 3 panos as context, FID scores improve 32.0 to 22.3. We notice similar gains for multi-step (1-6 steps) prediction. On Val-seen, we improve FID scores slightly over Pathdreamer but perform worse on multi-step prediction in Val-Seen environments. We attribute this anomaly to Pathdreamer’s recurrent training regime for their Structure Generator, under which the model is trained over multiple prediction steps while accumulating its own outputs as additional context. In initial experiments we found that this improved results in the training environments, but did not generalize to unseen environments, perhaps because the accumulated context from the model predictions doesn’t reconcile with the target image used in the  $L_1$  depth reconstruction loss. In unseen environments (which is our focus), our model performs better on FID score at every step. As shown in Fig. 2, despite using a far simpler model than Pathdreamer that does not require ground-truth semantic segmentation inputs, our model produces a clearer image of the wooden cabinet at 1.4m, the wooden ceiling rafters at 5.7m, and the passageway at 7.5m away.

*Human evaluations.* We perform human evaluations of 1,000 image pairs from our model and Pathdreamer. Each pair is evaluated by 5 different human evaluators, similar to the procedure in [36]. Since human evaluators may be unfamiliar with the distortion characteristics of 360° equirectangular images, for each pair evaluators are shown a random perspective projection from the generated images with 102° horizontal field-of-view and 16:9 aspect ratio. Images generated by our model are preferred over Pathdreamer images in 60.4% of cases (see Fig. 3). For images with unanimous preference (preferred by 5/5 raters), our model is greatly preferred: 30.7% compared to 12.3% for Pathdreamer.

## 4.2 Ablation Studies

To validate the design choices detailed in Sec. 3, we perform an extensive ablation study. FID scores on Matterport3D are summarized in Tab. 2.

*Loss functions.* We find that the adversarial loss and  $L_1$  depth reconstruction loss are both essential to strong performance: dropping the  $L_1$  loss (row 2) reduces

generation quality for 1 step ahead (FID@1 increases from 19.6 to 22.7), as well as over longer horizons (FID@{1-6} increases from 58.0 to 64.8). When we include the VGG perceptual loss [34] (row 3), we find that FID@1 is improved (19.6 to 18.2), but FID@{1-6} deteriorates (58.0 to 66.5). This is likely because visual quality is improved at the cost of RGB and depth consistency, which is essential for rollouts over multiple prediction steps. When KLD loss for stochastic noise conditioning [13,37] is included (row 4), generation quality worsens slightly for both 1 step and 1-6 steps ahead (FID@1 from 19.6 to 22.6, and FID@{1-6} from 58.0 to 65.2). While modeling stochasticity can be beneficial, we leave this out to maximize generation quality. Notably, even with the inclusion of the KLD loss and noise conditioning our results still outperform Pathdreamer, particularly in 1 step predictions (FID@1 of 22.6 vs. 27.2).

*Separate decoders.* As described in Sec. 3.2, we use a shared encoder with two separate decoders for RGB and depth. Using a single shared decoder (row 5) degrades generation quality for 1 step (FID@1 deteriorates from 19.6 to 24.1), although longer rollouts see slight improvement, improving FID@{1-6} from 58.0 to 56.9. This is likely due to marginally improved consistency between the RGB and depth outputs, which is essential for multistep prediction.

*Random masking and conv layers.* As described in Sec. 3.2, we insert 4 additional  $3 \times 3$  convolutional layers between the encoder and the decoders to increase the model’s receptive field and better propagate global image information. This is combined with random masking during training, where up to 75% of the guidance pixels are replaced with zeros. These changes significantly improve generation quality both in one-step predictions (FID@1 improves from 24.2 in row 6 to 19.6) and over multiple steps (FID@{1-6} improves from 68.0 to 58.0).

*Ground-truth depth for GAN loss.* During training, the adversarial GAN [20] hinge loss [40] is computed on the generated RGB-D image. We experimented with a version which instead replaces the generated depth channel with the ground-truth depth channel, to explore whether this would help enforce RGB and depth consistency. Our findings suggest that it does not, with FID@1 degrading from 19.6 to 24.3 and FID@{1-6} from 58.0 to 66.1.

### 4.3 RealEstate10K

*Training.* The RealEstate10K [78] dataset consists of a collection of YouTube walkthrough videos of real estate properties. Accordingly, in its raw form, the dataset lacks depth images and camera poses, which are required by our model to create point clouds and re-project guidance images. The PixelSynth [55] and SynSin [71] models, which we compare to, include a depth estimation module which is trained on the RE10K dataset using reprojection losses. We use MiDaS [52], a pretrained transformer-based monocular depth estimation model, and we do not finetune on RE10K. To estimate camera poses we use COLMAP [62],



Table 2: FID scores for ablations on Matterport3D, using 1 context image.

Row	Ablation	Val-Unseen	
		1 Step	1-6 Steps
1	Ours	19.6	58.0
2	– $L_1$ depth loss	22.7	64.8
3	+ VGG perceptual loss	18.2	66.5
4	+ KLD for noise conditioning	22.6	65.2
5	+ Shared decoder	24.1	56.9
6	– Random masking and conv layers	24.2	68.0
7	+ Ground-truth depth in GAN loss	24.3	66.1

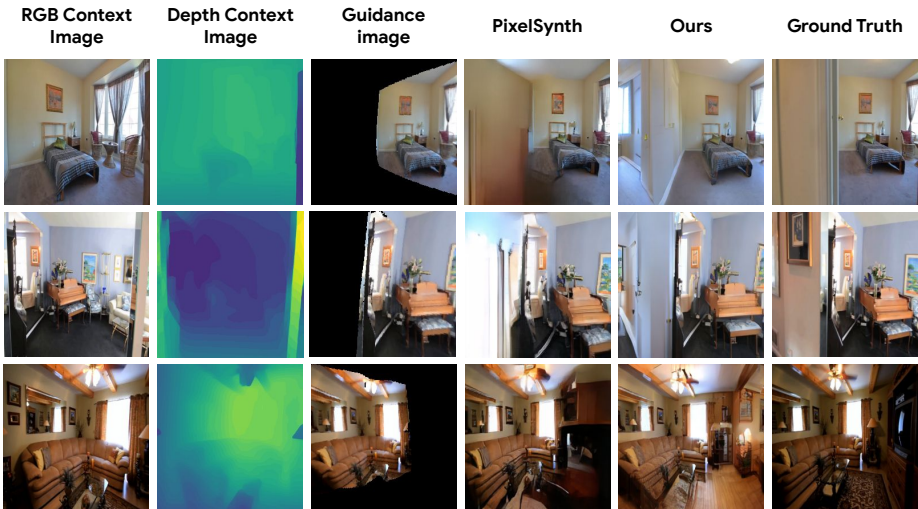


Fig. 4: Qualitative comparison of predictions on the RealEstate10K [80] dataset. In these selected examples, our model completes the scene by imagining adjacent rooms (Row 1, Row 2), while keeping wall and carpet colors consistent (Row 1), and introducing new elements like lamps and a wall painting (Row 3).

a standard structure-from-motion pipeline which we apply to RE10K video sequences. Since generating guidance images requires the camera poses and depth images to have a consistent scale – and the true scale of the scene is unrecoverable – during training we scale and bias the MiDaS depth estimates to match the depth estimates of the keypoints detected by COLMAP. As with the Matterport3D experiments, we train our model for single-step prediction, using a perspective camera projection for the guidance images rather than the equirectangular camera model used in Sec. 4.1. Following PixelSynth, we select image pairs for training with a camera rotation of  $20^\circ - 60^\circ$  that are estimated to be  $\leq 1m$  apart, and train and evaluate with an image resolution of  $256 \times 256$ .

*Evaluation.* Given an RGB context image and a target camera pose, the model must generate an RGB image for the target pose. We evaluate using the same



Table 3: FID scores ( $\downarrow$ ) over the RE10K validation set and a subset containing only indoor images.

Method	RE10K FID $\downarrow$	
	All	Indoors
SynSin [71]	34.7	-
PixelSynth [55]	25.5	23.6
Ours	<b>23.5</b>	<b>21.5</b>

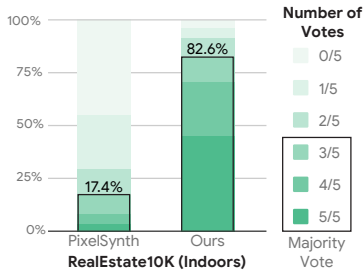


Fig. 5: Human evaluations ( $\uparrow$ ) comparing our model against PixelSynth on RE10K.

3,600 context-target image pairs and camera poses as PixelSynth. Since the scaling of the camera poses is arbitrary, during evaluation we scale the MiDaS depth predictions to match the PixelSynth depth predictions as closely as possible, so that the depth predictions and camera poses have consistent scaling. Qualitatively, the guidance images used by each model are extremely similar. We verify that none of the videos contributing evaluation images are in our training set.

*FID Scores.* As reported in Tab. 3, our model outperforms existing methods on this task, achieving an FID score of 23.5 compared to 25.5 and 34.7 achieved by PixelSynth [55] and SynSin [71] respectively. Notably, PixelSynth results were achieved by generating 50 sample target images for each input example, and ranking them according to a combination of discriminator loss and the entropy of a scene classifier trained on MIT Places 365 [77] to select the best. Our results represent a single prediction from our more simple model. Since we excluded outdoor scenes from our training data, we also report results on a subset of only indoor images (3,122 of the 3,600 images, based on manual inspection). On this subset, we achieve an FID score of 21.5 vs. 23.6 from PixelSynth.

*Human Evaluations.* We also performed human evaluations on this subset similar to the procedure we conduct on Matterport3D (Sec. 4.1). As shown in Fig. 5, human annotators significantly prefer images generated by our model over PixelSynth, rating them as more realistic in 77.3% of cases. In addition, for images which achieve unanimous preference (selected by 5/5 raters), our model is massively preferred, spanning 40.5% of images compared to just 3.5% for PixelSynth. Qualitative comparisons in Fig. 4 show that our model completes some of the scenes by imagining adjacent rooms (Row 1, Row 2), while keeping wall and carpet colors consistent (Row 1), and introducing new elements like lamps and a wall painting (Row 3).

## 5 Trajectory Augmentation in VLN

Motivated by our strong generation results, we investigate the usefulness of our model for synthetic *trajectory augmentation*, i.e., augmenting the training data

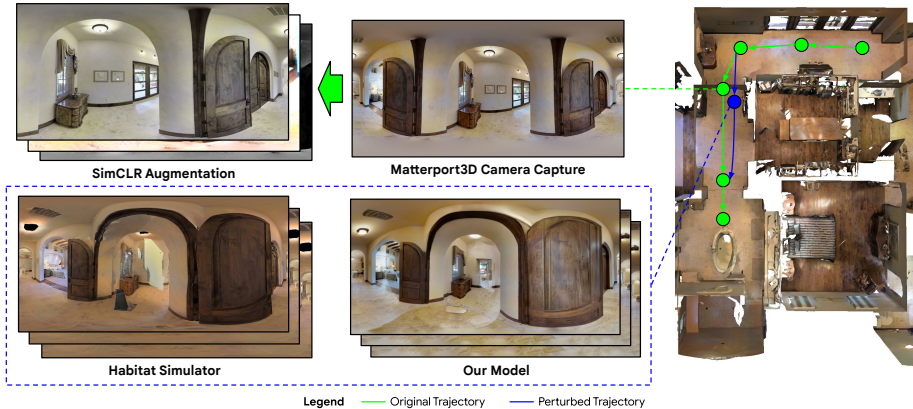


Fig. 6: VLN data augmentations, comparing SimCLR image-space augmentations to *trajectory augmentation* using our model and/or the Habitat simulator.

for a vision-based navigation robot by spatially perturbing collected training trajectories *post hoc*. We focus on vision-and-language navigation (VLN) using the Room-to-Room (R2R) dataset [2]. This task requires an agent to follow natural language navigation instructions in unseen photorealistic indoor environments, by navigating between locations where high-res 360° Matterport3D panos have been captured. Training data consists of 14K English instruction-trajectory pairs, where each trajectory is defined by a sequence of panos that are adjacent in a navigation graph. Constrained as they are by the location of captured images, VLN agents tend to overfit to the incidental details of these trajectories [76], which contributes to the significant performance drop in unseen environments (refer Tab. 5). We hypothesize that spatially perturbing the location of the captured images could reduce overfitting and improve generalization.

**VLN Agent and Metrics** We base our experiments on the VLN $\odot$ BERT agent [28], an image-text cross-modal transformer with a recurrent state that is updated over time as the agent moves. The agent is trained using a mixture of imitation learning and A2C [48]. To make the baseline as strong as possible, we first upgrade the image representation used by the model from ResNet-152 [24] trained on Places365 [77] to MURAL-large [31], an EfficientNet-B7 architecture [68] trained on 1.8B web image-text pairs. As illustrated in Tab. 4, this improves the agent’s Success Rate (SR  $\uparrow$ ) on the R2R Val-Unseen split from 62.2% to 67.3%, which beats even the recent *state-of-the-art* HAMT model [8]. SR is defined as the proportion of trajectories ending within 3m of the end of the target location. We also report Navigation Error (NE  $\downarrow$ ), the average distance in meters between the agent’s final position and the target, and Success rate weighted by the normalized inverse of the Path Length (SPL  $\uparrow$ ) [1].

**Trajectory Augmentation** To implement synthetic trajectory augmentation, we continually re-sample pano locations while training the VLN agent. We per-

Table 4: VLN performance on R2R [2] for our results extending VLN $\odot$ BERT, with results reported as best over the Val-Unseen set. Synthetic trajectories from our model can improve an already state-of-the-art model by up to 1.5% on Val-Unseen (Row 5, 6), while image-based data augmentations (Row 3) and simulator renders alone (Row 4) are ineffective.

# Model	Val-Seen			Val-Unseen		
	NE $\downarrow$	SR $\uparrow$	SPL $\uparrow$	NE $\downarrow$	SR $\uparrow$	SPL $\uparrow$
1. VLN $\odot$ BERT(retrained)	3.00	71.2	66.1	3.95	62.2	56.7
2. + MURAL [31]	<b>2.78</b>	<b>73.9</b>	<b>68.8</b>	3.58	67.3	60.9
3. + MURAL & SimCLR [9]	3.29	69.4	63.5	3.55	66.5	59.5
4. + MURAL & Habitat	3.45	65.1	60.3	3.47	66.8	60.7
5. + MURAL & Ours	3.09	71.3	65.6	3.41	68.1	<b>61.8</b>
6. + MURAL & Habitat & Ours	3.29	68.2	62.7	<b>3.29</b>	<b>68.8</b>	61.5

Table 5: VLN results on R2R [2] comparing against best performing prior work.

Model	Val-Seen			Val-Unseen			Test-Unseen		
	NE $\downarrow$	SR $\uparrow$	SPL $\uparrow$	NE $\downarrow$	SR $\uparrow$	SPL $\uparrow$	NE $\downarrow$	SR $\uparrow$	SPL $\uparrow$
Fast-Short [43]	-	-	-	4.97	56	43	5.14	54	41
EnvDrop [67]	3.99	62.1	59	5.22	52.2	48	5.23	51	47
PREVALENT [22]	3.67	69	65	4.71	58	53	5.30	54	51
RelGraph [27]	3.47	67	65	4.73	57	53	4.75	55	52
VLN $\odot$ BERT [28]	2.90	72	68	3.93	63	57	4.09	63	57
HAMT [8]	<b>2.51</b>	<b>76</b>	<b>72</b>	<b>2.29</b>	66	61	3.93	65	<b>60</b>
VLN $\odot$ BERT(MURAL) + Habitat + Ours	3.29	68	63	3.29	<b>69</b>	<b>62</b>	<b>3.67</b>	<b>66</b>	<b>60</b>

turb the agent’s position with a translation sampled uniformly at random from  $(-1.5\text{m}, 1.5\text{m})$  for directions parallel to the ground plane and from  $(-0.1\text{m}, 0.1\text{m})$  for height. To avoid perturbing the pano location through a wall or inside an object, we reject any perturbation that exceeds the depth returned in that direction. The pano is generated at  $1024 \times 512$  resolution by our model trained on Matterport3D, using the nearest two ground-truth RGB-D panos as context. We compare this approach to two alternatives: (1) image space data augmentation using SimCLR [9], a carefully tuned composition of random cropping, color distortion and Gaussian blur operations, and (2) rendering the spatially-perturbed pano from the Matterport3D textured mesh using the Habitat [61] simulator.

*Results* As shown in Tab. 4, trajectory augmentation using our model improves the agent’s SR and SPL on Val-Unseen by 1% (Row 5 vs Row 2), reducing the gap between Val-Seen and Val-Unseen from 8% to 4%. In contrast, SimCLR image-based data augmentation (Row 3) and textured mesh based renders using Habitat (Row 4) produce no improvements over the upgraded model (Row 2). Trajectory augmentation using a combination of Habitat and our model (Row 6) produced the largest improvement in SR (+1.5%), virtually closing the gap between Val-Seen and Val-Unseen performance, and on the unseen test set this model outperforms all published prior work (Tab. 5). The R2R dataset [2] is a mature benchmark at this time, and such gains do not come easily. Unlike Pathdreamer [37], which requires integration at inference time, our visual aug-

mentation procedure is completely training based, and this can be applied to train virtually any off-the-shelf VLN agent.

## 6 Conclusion

Synthesizing immersive 3D environments from limited images is a challenging task brought into focus by several recent concurrent works. These approaches are highly complex, with many separately trained stages and components. We propose a simple alternative: an image-to-image GAN trained with random input masking combined with small architecture changes. Perhaps surprisingly, our approach outperforms prior work in human evaluations and on FID, and its useful for generative data augmentation as well. We achieve state-of-the-art results on the R2R dataset by spatially perturbing the training images with our model, improving generalization to unseen environments.

## Acknowledgements

We would like to thank Noah Snaveley and many others for their insightful ideas and discussions during the development of this paper. We thank Chris Rockwell for helping to set up PixelSynth models for comparison. We would also like to thank the Google ML Data Operations team for collecting human evaluations on our generated images.

## References

1. Anderson, P., Chang, A., Chaplot, D.S., Dosovitskiy, A., Gupta, S., Koltun, V., Kosecka, J., Malik, J., Mottaghi, R., Savva, M., Zamir, A.R.: On evaluation of embodied navigation agents. arXiv preprint arXiv:1807.06757 (2018)
2. Anderson, P., Wu, Q., Teney, D., Bruce, J., Johnson, M., Sünderhauf, N., Reid, I., Gould, S., van den Hengel, A.: Vision-and-language navigation: Interpreting visually-grounded navigation instructions in real environments. In: CVPR. pp. 3674–3683 (2018)
3. Antoniou, A., Storkey, A., Edwards, H.: Data augmentation generative adversarial networks. arXiv preprint arXiv:1711.04340 (2017)
4. Avidan, S., Shashua, A.: Novel view synthesis in tensor space. In: Proceedings of IEEE Computer Society Conference on Computer Vision and Pattern Recognition. pp. 1034–1040. IEEE (1997)
5. Barron, J.T., Mildenhall, B., Tancik, M., Hedman, P., Martin-Brualla, R., Srinivasan, P.P.: Mip-nerf: A multiscale representation for anti-aliasing neural radiance fields. arXiv preprint arXiv:2103.13415 (2021)
6. Bojarski, M., Del Testa, D., Dworakowski, D., Firner, B., Flepp, B., Goyal, P., Jackel, L.D., Monfort, M., Muller, U., Zhang, J., et al.: End to end learning for self-driving cars. arXiv:1604.07316 (2016)
7. Chang, A., Dai, A., Funkhouser, T., Halber, M., Niessner, M., Savva, M., Song, S., Zeng, A., Zhang, Y.: Matterport3d: Learning from RGB-D data in indoor environments. International Conference on 3D Vision (3DV) (2017)

8. Chen, S., Guhur, P.L., Schmid, C., Laptev, I.: History aware multimodal transformer for vision-and-language navigation. In: NeurIPS (2021)
9. Chen, T., Kornblith, S., Norouzi, M., Hinton, G.: A simple framework for contrastive learning of visual representations (2020)
10. Codevilla, F., Müller, M., López, A., Koltun, V., Dosovitskiy, A.: End-to-end driving via conditional imitation learning. In: ICRA (2018)
11. Cortinhal, T., Kurnaz, F., Aksoy, E.E.: Semantics-aware multi-modal domain translation: From lidar point clouds to panoramic color images. In: Proceedings of the IEEE/CVF International Conference on Computer Vision. pp. 3032–3048 (2021)
12. Debevec, P.E., Taylor, C.J., Malik, J.: Modeling and rendering architecture from photographs: A hybrid geometry-and image-based approach. In: Proceedings of the 23rd annual conference on Computer graphics and interactive techniques. pp. 11–20 (1996)
13. Denton, E., Fergus, R.: Stochastic video generation with a learned prior (2018)
14. Dhama, H., Tateno, K., Laina, I., Navab, N., Tombari, F.: Peeking behind objects: Layered depth prediction from a single image. *Pattern Recognition Letters* **125**, 333–340 (2019)
15. Dosovitskiy, A., Beyer, L., Kolesnikov, A., Weissenborn, D., Zhai, X., Unterthiner, T., Dehghani, M., Minderer, M., Heigold, G., Gelly, S., et al.: An image is worth 16x16 words: Transformers for image recognition at scale. arXiv preprint arXiv:2010.11929 (2020)
16. Finn, C., Levine, S.: Deep visual foresight for planning robot motion. In: ICRA (2017)
17. Flynn, J., Broxton, M., Debevec, P., DuVall, M., Fyffe, G., Overbeck, R., Snavely, N., Tucker, R.: Deepview: View synthesis with learned gradient descent. In: CVPR. pp. 2367–2376 (2019)
18. Flynn, J., Neulander, I., Philbin, J., Snavely, N.: Deepstereo: Learning to predict new views from the world’s imagery. In: CVPR (2016)
19. Fu, Z., Hu, W., Guo, Z.: 3d dynamic point cloud inpainting via temporal consistency on graphs. In: 2020 IEEE International Conference on Multimedia and Expo (ICME). pp. 1–6. IEEE (2020)
20. Goodfellow, I.J., Pouget-Abadie, J., Mirza, M., Xu, B., Warde-Farley, D., Ozair, S., Courville, A., Bengio, Y.: Generative adversarial networks. *NeurIPS* (2014)
21. Ha, D., Schmidhuber, J.: World models. *NeurIPS* (2018)
22. Hao, W., Li, C., Li, X., Carin, L., Gao, J.: Towards learning a generic agent for vision-and-language navigation via pre-training. In: CVPR (June 2020)
23. He, K., Chen, X., Xie, S., Li, Y., Dollár, P., Girshick, R.: Masked autoencoders are scalable vision learners. arXiv preprint arXiv:2111.06377 (2021)
24. He, K., Zhang, X., Ren, S., Sun, J.: Deep residual learning for image recognition. In: CVPR. pp. 770–778 (2016)
25. Henzler, P., Rasche, V., Ropinski, T., Ritschel, T.: Single-image tomography: 3d volumes from 2d cranial x-rays. In: *Computer Graphics Forum*. vol. 37, pp. 377–388. Wiley Online Library (2018)
26. Heusel, M., Ramsauer, H., Unterthiner, T., Nessler, B., Hochreiter, S.: GANs trained by a two time-scale update rule converge to a local nash equilibrium. In: *NeurIPS* (2017)
27. Hong, Y., Rodriguez, C., Qi, Y., Wu, Q., Gould, S.: Language and visual entity relationship graph for agent navigation (2020)
28. Hong, Y., Wu, Q., Qi, Y., Rodriguez-Opazo, C., Gould, S.: A recurrent vision-and-language BERT for navigation. In: *ECCV* (2021)

29. Hu, R., Ravi, N., Berg, A.C., Pathak, D.: Worldsheet: Wrapping the world in a 3d sheet for view synthesis from a single image. In: Proceedings of the IEEE/CVF International Conference on Computer Vision. pp. 12528–12537 (2021)
30. Isola, P., Zhu, J.Y., Zhou, T., Efros, A.A.: Image-to-image translation with conditional adversarial networks. CVPR (2017)
31. Jain, A., Guo, M., Srinivasan, K., Chen, T., Kudugunta, S., Jia, C., Yang, Y., Baldridge, J.: Mural: Multimodal, multitask retrieval across languages. In: arXiv:2109.05125 (2021)
32. Jain, A., Tancik, M., Abbeel, P.: Putting nerf on a diet: Semantically consistent few-shot view synthesis. In: Proceedings of the IEEE/CVF International Conference on Computer Vision. pp. 5885–5894 (2021)
33. Jiang, J., Zheng, L., Luo, F., Zhang, Z.: Rednet: Residual encoder-decoder network for indoor rgb-d semantic segmentation. arXiv preprint arXiv:1806.01054 (2018)
34. Johnson, J., Alahi, A., Fei-Fei, L.: Perceptual losses for real-time style transfer and super-resolution. In: ECCV. pp. 694–711 (2016)
35. Kar, A., Häne, C., Malik, J.: Learning a multi-view stereo machine. In: NeurIPS. pp. 365–376 (2017)
36. Koh, J.Y., Baldridge, J., Lee, H., Yang, Y.: Text-to-image generation grounded by fine-grained user attention. In: Proceedings of the IEEE/CVF Winter Conference on Applications of Computer Vision. pp. 237–246 (2021)
37. Koh, J.Y., Lee, H., Yang, Y., Baldridge, J., Anderson, P.: Pathdreamer: A world model for indoor navigation. In: ICCV (2021)
38. Li, Z., Dekel, T., Cole, F., Tucker, R., Snaveley, N., Liu, C., Freeman, W.T.: Mannequinchallenge: Learning the depths of moving people by watching frozen people. TPAMI (2021)
39. Li, Z., Snaveley, N.: Megadepth: Learning single-view depth prediction from internet photos. In: Proceedings of the IEEE Conference on Computer Vision and Pattern Recognition. pp. 2041–2050 (2018)
40. Lim, J.H., Ye, J.C.: Geometric gan. arXiv preprint arXiv:1705.02894 (2017)
41. Liu, A., Tucker, R., Jampani, V., Makadia, A., Snaveley, N., Kanazawa, A.: Infinite nature: Perpetual view generation of natural scenes from a single image. In: Proceedings of the IEEE/CVF International Conference on Computer Vision. pp. 14458–14467 (2021)
42. Liu, G., Reda, F.A., Shih, K.J., Wang, T.C., Tao, A., Catanzaro, B.: Image inpainting for irregular holes using partial convolutions. In: ECCV. pp. 85–100 (2018)
43. Liyiming Ke, Xiujun Li, Y.B.A.H.Z.G.J.L.J.G.Y.C.S.S.: Tactical rewind: Self-correction via backtracking in vision-and-language navigation. In: CVPR (2019)
44. Mallya, A., Wang, T.C., Sapra, K., Liu, M.Y.: World-consistent video-to-video synthesis. ECCV (2020)
45. Martin-Brualla, R., Radwan, N., Sajjadi, M.S.M., Barron, J.T., Dosovitskiy, A., Duckworth, D.: NeRF in the Wild: Neural Radiance Fields for Unconstrained Photo Collections. In: CVPR (2021)
46. Mildenhall, B., Srinivasan, P.P., Ortiz-Cayon, R., Kalantari, N.K., Ramamoorthi, R., Ng, R., Kar, A.: Local light field fusion: Practical view synthesis with prescriptive sampling guidelines. ACM Transactions on Graphics (TOG) **38**(4), 1–14 (2019)
47. Mildenhall, B., Srinivasan, P.P., Tancik, M., Barron, J.T., Ramamoorthi, R., Ng, R.: Nerf: Representing scenes as neural radiance fields for view synthesis. ECCV (2020)

48. Mnih, V., Badia, A.P., Mirza, M., Graves, A., Lillicrap, T., Harley, T., Silver, D., Kavukcuoglu, K.: Asynchronous methods for deep reinforcement learning. In: ICML (2016)
49. Mur-Artal, R., Montiel, J.M.M., Tardós, J.D.: Orb-slam: A versatile and accurate monocular slam system. *IEEE Transactions on Robotics* **31**, 1147–1163 (2015)
50. Nathan Silberman, Derek Hoiem, P.K., Fergus, R.: Indoor segmentation and support inference from rgb-d images. In: ECCV (2012)
51. Park, T., Liu, M.Y., Wang, T.C., Zhu, J.Y.: Semantic image synthesis with spatially-adaptive normalization. In: CVPR. pp. 2337–2346 (2019)
52. Ranftl, R., Bochkovskiy, A., Koltun, V.: Vision transformers for dense prediction. ArXiv preprint (2021)
53. Razavi, A., van den Oord, A., Vinyals, O.: Generating diverse high-fidelity images with vq-vae2 (2019)
54. Ren, X., Wang, X.: Look outside the room: Synthesizing a consistent long-term 3d scene video from a single image. In: CVPR (2022)
55. Rockwell, C., Fouhey, D.F., Johnson, J.: Pixelsynth: Generating a 3d-consistent experience from a single image. In: Proceedings of the IEEE/CVF International Conference on Computer Vision. pp. 14104–14113 (2021)
56. Rombach, R., Esser, P., Ommer, B.: Geometry-free view synthesis: Transformers and no 3d priors. In: Proceedings of the IEEE/CVF International Conference on Computer Vision (2021)
57. Ross, S., Bagnell, D.: Efficient reductions for imitation learning. In: Proceedings of the thirteenth international conference on artificial intelligence and statistics. pp. 661–668. JMLR Workshop and Conference Proceedings (2010)
58. Salimans, T., Karpathy, A., Chen, X., Kingma, D.P.: Pixelcnn++: Improving the pixelcnn with discretized logistic mixture likelihood and other modifications. ICLR (2017)
59. Sandfort, V., Yan, K., Pickhardt, P.J., Summers, R.M.: Data augmentation using generative adversarial networks (cycleGAN) to improve generalizability in ct segmentation tasks. *Scientific reports* **9**(1), 1–9 (2019)
60. Savva, M., Kadian, A., Maksymets, O., Zhao, Y., Wijmans, E., Jain, B., Straub, J., Liu, J., Koltun, V., Malik, J., Parikh, D., Batra, D.: Habitat: A Platform for Embodied AI Research. In: ICCV (2019)
61. Savva, M., Kadian, A., Maksymets, O., Zhao, Y., Wijmans, E., Jain, B., Straub, J., Liu, J., Koltun, V., Malik, J., et al.: Habitat: A platform for embodied ai research. In: Proceedings of the IEEE/CVF International Conference on Computer Vision. pp. 9339–9347 (2019)
62. Schönberger, J.L., Frahm, J.M.: Structure-from-motion revisited. In: Conference on Computer Vision and Pattern Recognition (CVPR) (2016)
63. Shih, M.L., Su, S.Y., Kopf, J., Huang, J.B.: 3d photography using context-aware layered depth inpainting. In: CVPR (June 2020)
64. Shih, M.L., Su, S.Y., Kopf, J., Huang, J.B.: 3d photography using context-aware layered depth inpainting. In: Proceedings of the IEEE/CVF Conference on Computer Vision and Pattern Recognition. pp. 8028–8038 (2020)
65. Song, Z., Chen, W., Campbell, D., Li, H.: Deep novel view synthesis from colored 3d point clouds. In: European Conference on Computer Vision. pp. 1–17. Springer (2020)
66. Srinivasan, P.P., Tucker, R., Barron, J.T., Ramamoorthi, R., Ng, R., Snavely, N.: Pushing the boundaries of view extrapolation with multiplane images. In: CVPR. pp. 175–184 (2019)



67. Tan, H., Yu, L., Bansal, M.: Learning to navigate unseen environments: Back translation with environmental dropout. In: Proceedings of the 2019 Conference of the North American Chapter of the Association for Computational Linguistics: Human Language Technologies, Volume 1 (Long and Short Papers). pp. 2610–2621 (2019)
68. Tan, M., Le, Q.: EfficientNet: Rethinking model scaling for convolutional neural networks (2019)
69. Tancik, M., Casser, V., Yan, X., Pradhan, S., Mildenhall, B., Srinivasan, P.P., Barron, J.T., Kretschmar, H.: Block-nerf: Scalable large scene neural view synthesis. arXiv preprint arXiv:2202.05263 (2022)
70. Tucker, R., Snavely, N.: Single-view view synthesis with multiplane images. In: CVPR. pp. 551–560 (2020)
71. Wiles, O., Gkioxari, G., Szeliski, R., Johnson, J.: Synsin: End-to-end view synthesis from a single image. In: CVPR. pp. 7467–7477 (2020)
72. Xia, F., R. Zamir, A., He, Z.Y., Sax, A., Malik, J., Savarese, S.: Gibson Env: real-world perception for embodied agents. In: CVPR. IEEE (2018)
73. Xia, F., Zamir, A.R., He, Z., Sax, A., Malik, J., Savarese, S.: Gibson env: Real-world perception for embodied agents. In: Proceedings of the IEEE conference on computer vision and pattern recognition. pp. 9068–9079 (2018)
74. Yu, A., Ye, V., Tancik, M., Kanazawa, A.: pixelnerf: Neural radiance fields from one or few images. arXiv preprint arXiv:2012.02190 (2020)
75. Yu, Y., Huang, Z., Li, F., Zhang, H., Le, X.: Point encoder gan: A deep learning model for 3d point cloud inpainting. *Neurocomputing* **384**, 192–199 (2020)
76. Zhang, Y., Tan, H., Bansal, M.: Diagnosing the environment bias in vision-and-language navigation. *IJCAI* (2020)
77. Zhou, B., Lapedriza, À., Khosla, A., Oliva, A., Torralba, A.: Places: A 10 million image database for scene recognition. *IEEE Transactions on Pattern Analysis and Machine Intelligence* **40**, 1452–1464 (2018)
78. Zhou, T., Tucker, R., Flynn, J., Fyffe, G., Snavely, N.: Stereo magnification: Learning view synthesis using multiplane images. *ACM Trans. Graph. (Proc. SIGGRAPH)* **37** (2018), <https://arxiv.org/abs/1805.09817>
79. Zhou, T., Tucker, R., Flynn, J., Fyffe, G., Snavely, N.: Stereo magnification: Learning view synthesis using multiplane images. *SIGGRAPH* (2018)
80. Zhou, T., Tucker, R., Flynn, J., Fyffe, G., Snavely, N.: Stereo magnification: Learning view synthesis using multiplane images (2018)
81. Zitnick, C.L., Kang, S.B., Uyttendaele, M., Winder, S., Szeliski, R.: High-quality video view interpolation using a layered representation. *ACM transactions on graphics (TOG)* **23**(3), 600–608 (2004)

## A Implementation Details

*Training Details.* All models are implemented in TensorFlow 2.0. We set loss weights  $\lambda_{\text{GAN}} = 1.0$  and  $\lambda_{\text{D}} = 100.0$ . Spectral normalization is used for all convolutional layers in the generator and discriminator. We train using the Adam optimizer with parameters  $\beta_1 = 0.5$  and  $\beta_2 = 0.999$ . The learning rates for the generator and discriminator are set to  $1e^{-4}$  and  $4e^{-4}$  respectively. The discriminator is trained for two training steps for each training step of the generator. For evaluation, we apply exponential moving average of generator weights with decay of 0.999. All models are trained for 300K steps with a batch size of 128, and early stopping is applied based on FID scores on the validation dataset.

*Evaluation Details.* For Matterport3D, we follow Pathdreamer to compute the FID score<sup>6</sup> using 10,000 random samples for each prediction sequence step. Random horizontal roll and flips are applied to obtain 10,000 samples for evaluation.

For RealEstate10K, we follow PixelSynth in computing the FID score over their evaluation set of 3,600 examples. As our training data does not contain outdoor images, we extract a subset of only indoor images (3,122 out of 3,600) based on an image classifier. We classifier frames as indoors if they are tagged with any of the ‘room’, ‘floor’, ‘kitchen’, ‘table’, ‘sofa’, ‘bed’ categories. We manually inspected images which had uncertain predictions. We ran the same evaluation on this subset of 3,122 images for both our model and PixelSynth.

## B Architectural Details

The detailed generator and discriminator architectures for our model can be found in Tab. 6a and Tab. 6b respectively. The same architecture is used for both Matterport3D and RealEstate10K, with the exception of the input size  $H \times W$  being changed to the appropriate input dimensions ( $1024 \times 512$  and  $256 \times 256$  respectively). All convolutions used in the encoder ResNet-101 are partial convolutions.

<b>Input:</b> Context RGB-D and camera poses $(I_{1:t-1}, d_{1:t-1}, P_{1:t-1})$	<b>Input:</b> $x = \text{real/fake RGB-D images } [I_i, d_i] \in \mathbb{R}^{H \times W \times 4}$
$(I_{1:t-1}, d_{1:t-1}, P_{1:t-1}) \rightarrow \text{Reprojection to } P_t \rightarrow x_{\text{guidance}}$	$x \rightarrow 4 \times 4 \text{ Conv} \rightarrow \text{LeakyReLU} \rightarrow (H/2, W/2, 128)$
$x_{\text{guidance}} \rightarrow \text{ResNet-101} \rightarrow (H//32, W//32, 512)$	$4 \times 4 \text{ Conv} \rightarrow \text{InstanceNorm} \rightarrow \text{LeakyReLU} \rightarrow (H/4, W/4, 256)$
$\text{BatchNorm} \rightarrow 3 \times 3 \text{ Conv} \rightarrow \text{LeakyReLU} \rightarrow (H//32, W//32, 512)$	$4 \times 4 \text{ Conv} \rightarrow \text{InstanceNorm} \rightarrow \text{LeakyReLU} \rightarrow (H/8, W/8, 512)$
$\text{BatchNorm} \rightarrow 3 \times 3 \text{ Conv} \rightarrow \text{LeakyReLU} \rightarrow (H//32, W//32, 1024)$	$4 \times 4 \text{ Conv} \rightarrow \text{InstanceNorm} \rightarrow \text{LeakyReLU} \rightarrow (H/16, W/16, 512)$
$\text{BatchNorm} \rightarrow 3 \times 3 \text{ Conv} \rightarrow \text{LeakyReLU} \rightarrow (H//32, W//32, 512)$	$4 \times 4 \text{ Conv} \rightarrow \text{InstanceNorm} \rightarrow \text{LeakyReLU} \rightarrow (H/32, W/32, 512)$
$\text{BatchNorm} \rightarrow 3 \times 3 \text{ Conv} \rightarrow \text{LeakyReLU} \rightarrow (H//32, W//32, 512)$	$4 \times 4 \text{ Conv} \rightarrow \text{InstanceNorm} \rightarrow \text{LeakyReLU} \rightarrow (H/32, W/32, 512)$
$\text{BatchNorm} \rightarrow 3 \times 3 \text{ Conv} \rightarrow h_1, (H//32, W//32, 512)$	$4 \times 4 \text{ Conv} \rightarrow \text{Out1}, (H/32, W/32, 1)$
$h_1 \rightarrow \text{TransposedResNet-101}_D \rightarrow (H, W, 128)$	$x \rightarrow 3 \times 3 \text{ stride } 2 \text{ AvgPool} \rightarrow x_1, (H/2, W/2, 4)$
$\text{BatchNorm} \rightarrow 3 \times 3 \text{ Conv} \rightarrow \text{LeakyReLU} \rightarrow (H, W, 128)$	$x_1 \rightarrow 4 \times 4 \text{ Conv} \rightarrow \text{LeakyReLU} \rightarrow (H/4, W/4, 128)$
$\text{BatchNorm} \rightarrow 3 \times 3 \text{ Conv} \rightarrow \text{LeakyReLU} \rightarrow (H, W, 128)$	$4 \times 4 \text{ Conv} \rightarrow \text{InstanceNorm} \rightarrow \text{LeakyReLU} \rightarrow (H/8, W/8, 256)$
$\text{BatchNorm} \rightarrow 3 \times 3 \text{ Conv} \rightarrow d_t, (H, W, 1)$	$4 \times 4 \text{ Conv} \rightarrow \text{InstanceNorm} \rightarrow \text{LeakyReLU} \rightarrow (H/16, W/16, 512)$
$h_1 \rightarrow \text{TransposedResNet-101}_{\text{RGB}} \rightarrow (H, W, 128)$	$4 \times 4 \text{ Conv} \rightarrow \text{InstanceNorm} \rightarrow \text{LeakyReLU} \rightarrow (H/32, W/32, 512)$
$\text{BatchNorm} \rightarrow 3 \times 3 \text{ Conv} \rightarrow \text{LeakyReLU} \rightarrow (H, W, 128)$	$4 \times 4 \text{ Conv} \rightarrow \text{InstanceNorm} \rightarrow \text{LeakyReLU} \rightarrow (H/64, W/64, 512)$
$\text{BatchNorm} \rightarrow 3 \times 3 \text{ Conv} \rightarrow \text{LeakyReLU} \rightarrow (H, W, 128)$	$4 \times 4 \text{ Conv} \rightarrow \text{InstanceNorm} \rightarrow \text{LeakyReLU} \rightarrow (H/64, W/64, 512)$
$\text{BatchNorm} \rightarrow 3 \times 3 \text{ Conv} \rightarrow \hat{I}_t, (H, W, 3)$	$4 \times 4 \text{ Conv} \rightarrow \text{Out2}, (H/64, W/64, 1)$
<b>Final output:</b> $\hat{I}_t, (H, W, 3), d_t, (H, W, 1)$	<b>Final output:</b> $(\text{Out1} + \text{Out2})/2$

(a) Generator

(b) Discriminator

Table 6: Generator and discriminator architectures.

<sup>6</sup> We used <https://github.com/mseitzer/pytorch-fid> for computing results.

## C COLMAP sampling details

Now, we describe the details of our RealEstate10K training dataset. We obtain camera trajectories and depth maps for Youtube videos listed by running SLAM and bundle adjustment on the video frames. RealEstate10K [80] breaks down the YouTube video into a collection of smaller sub-sequences. Each sub-sequence consists of connected frames that were tracked by ORB-SLAM [49]. Out of the original dataset, only 6,865 videos are available because the rest have been taken down since the release. We ran the original pipeline from [80] but with longer sequence length (up to 1,000 frames) which results in a total of 108,275 sub-sequences containing over 19 million frames. Videos in the RealEstate10K dataset often contain walkthroughs of outdoor surroundings as well. Since we are only interested in synthesizing indoor scenes, we filter sub-sequences which contain outdoor frames from our dataset. We filter these by running a multi-label classifier which tags each frame of the sub-sequence with relevant semantic categories. We remove those sub-sequences in which no frame is tagged with any of the ‘room’, ‘floor’, ‘kitchen’, ‘table’, ‘sofa’, ‘bed’ categories. After filtering, we are left with 83,559 sub-sequences containing over 15 million frames. We obtain camera trajectories corresponding to each sub-sequence by running COLMAP [62], a structure-from-motion pipeline. COLMAP was able to successfully build dense reconstruction for 67,834 out of the 83,559 sub-sequences.

To obtain per-frame depth maps, we use a standard multi-view stereo (MVS) system in COLMAP. The depth estimates from MVS are often too noisy due to camera-blur, reflections, poor lightning, and other factors [38]. Following the procedure outlined in Li *et al.* [38], we first filter outlier depth values using the depth refinement method outlined in [39]. Next, we remove erroneous depth values by considering the consistency between MVS depth and depth obtained from motion parallax between adjacent pair of frames. Depth estimates from MVS has another limitation. These depth estimates are often extremely sparse. This severely limit the density of point-cloud constructed from context images, and leads to sparse guidance images for the model. To overcome this, we generate dense depth predictions from MiDaS [52]. MiDaS is a state-of-the-art transformer based monocular depth estimation model which outputs a dense depth map from a single RGB image. Of course, the scale of the depth predictions from MiDaS for different frames are inconsistent and not aligned with the camera pose. Thus they cannot be used to create a unified point-cloud. We tackle this by a simple fix. We scale the depth predictions from MiDaS to match the COLMAP MVS depth outputs for valid pixels using the least-squares method. We select only those frames for training for which the depth map produced by MVS covers at least 10% of the image.

## D Human evaluations

### D.1 User Interface and Process

We perform human evaluations of 1,000 image pairs for both the Matterport3D and RealEstate10K datasets. For Matterport3D, we do head-to-head compar-

**Task : Evaluate the given images and rate them in order**

Please select the image that looks more realistic overall. If you are unsure, select whichever image you prefer.



1. Which image is more realistic?

Rating : 1st (Best)

Rating : 2nd

Submit

Fig. 7: User interface shown to human raters for evaluating models on Matterport3D and RealEstate10K. Models are anonymized and shown in random order.

isons between our model and Pathdreamer, and for RealEstate10K, we compare our model against PixelSynth. Each pair is evaluated by 5 independent human evaluators, and the user interface is shown in Fig. 7. The two models are anonymized and shown in random order to minimize biases.

## D.2 Evaluation with Guidance Image

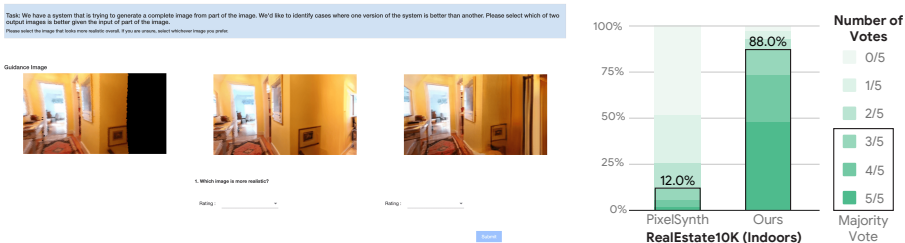


Fig. 8: User interface shown to human raters for performing evaluations RealEstate10K with guidance input (left), and human evaluations ( $\uparrow$ ) comparing our model to PixelSynth (right).

In addition to the evaluation described in our main paper and in Appendix D.1, we perform a secondary evaluation for RealEstate10K similar to the process in

PixelSynth. In this setup, we show the input guidance image to the evaluators, and task them to select the image that best matches the partial input (see Fig. 8). Under this procedure, we expect the evaluators to focus even more on the regions of the image requiring inpainting. Under this setting, our model significantly outperforms PixelSynth, with 88.0% of examples being preferred by human evaluators (compared to 12% for PixelSynth). For examples with unanimous preference (5/5 raters prefer it), our model is overwhelming preferred: 48.4% compared to 2.0% for PixelSynth.

## E Qualitative Evaluation

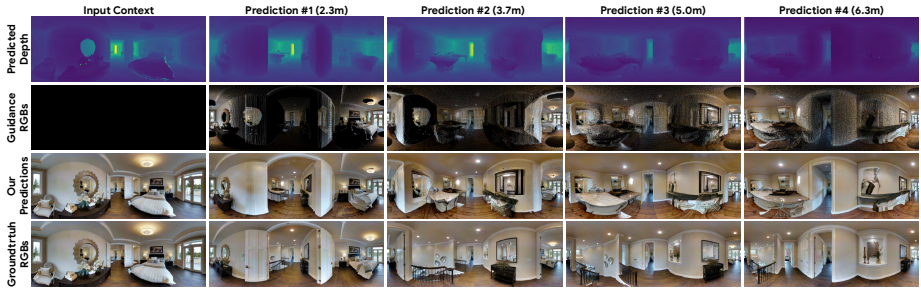
In this section, we present additional qualitative results generated by our model. We show cherry-picked examples (Fig. 9) and random examples (Fig. 10) on the Matterport3D dataset. Similarly, for the RealEstate10K dataset we show more cherry-picked examples (Fig. 13) and random examples (Fig. 14). We also provide more side-by-side comparisons of our model against Pathdreamer in Fig. 12.

### E.1 Video Generation Results

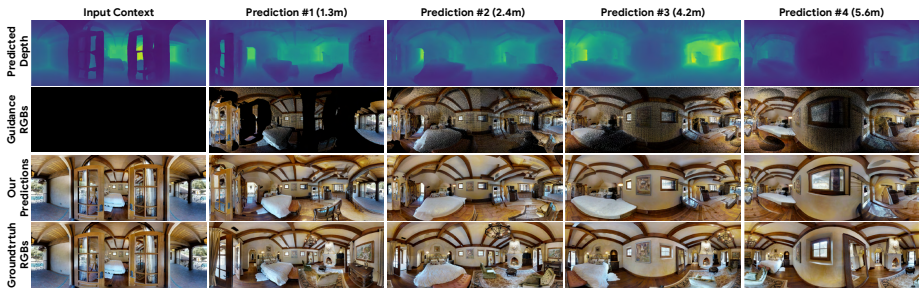
Our model is also capable of generating compelling, high resolution video by subsampling trajectories with small viewpoint changes. We provide videos displaying generation results for unseen environments in Matterport3D, and for rotations and camera trajectories from RealEstate10K. We refer readers to the anonymized YouTube link<sup>7</sup> for these results.

---

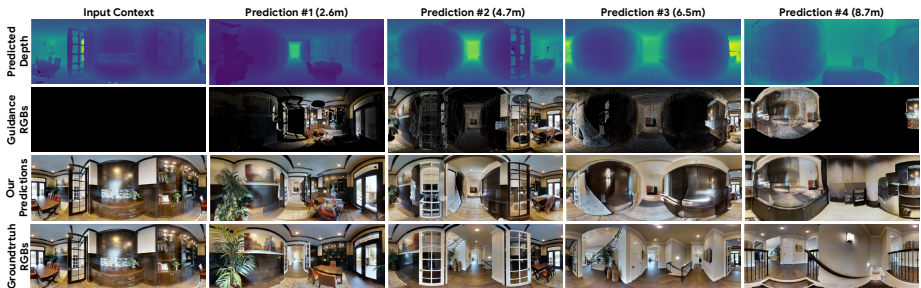
<sup>7</sup> Video results: <https://youtu.be/lhw1rRfFp0>



(a) At 2.3m, our model infills the missing region to hallucinate a table, which remains consistent at the following step (3.7m) and beyond. Even at 6.3m away, the 3D geometry (e.g., the doorway) of the scene is well preserved.



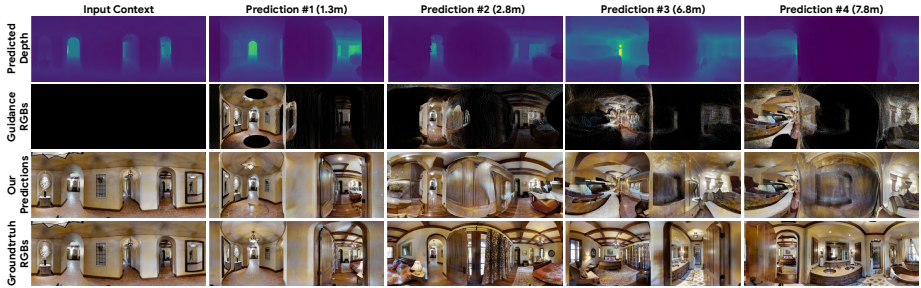
(b) At 1.3m, our model provides a plausible infilling of the missing regions of the scene, enabling accurate and geometrically consistent generation at future steps. Even at 5.6m away, the room generation results remain plausible.



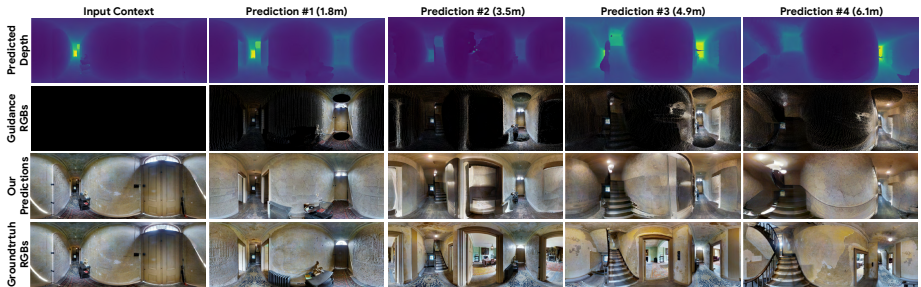
(c) Our model preserves high frequency textures well, as seen by the upscaling and generation of the plant at 2.6m. Our model also correctly infills the content of the doorway in the center at 2.6m, enabling plausible predictions at 4.7m and beyond.

Fig. 9: Selected examples of predicted sequences from the Val-Unseen R2R split of Matterport3D using one ground truth observation as context.

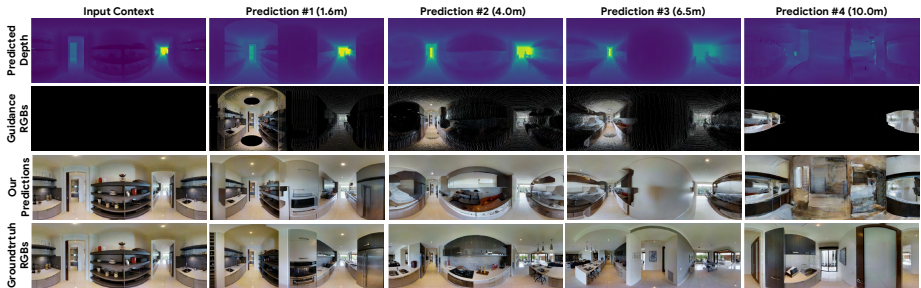




(a) At 1.3m, our model infills and completes the scene, generating an image that matches the groundtruth geometry very closely. This enables simulated traversal through the scene, producing fairly plausible generation results even at 6.8m and beyond.



(b) Our model is able to predict plausible generation results that respect the geometry of this hallway, including upsampling of the stairwell at step 3.5m. Although the model does not generate the room from the groundtruth at 4.9m, it generates a plausible result assuming a wall.



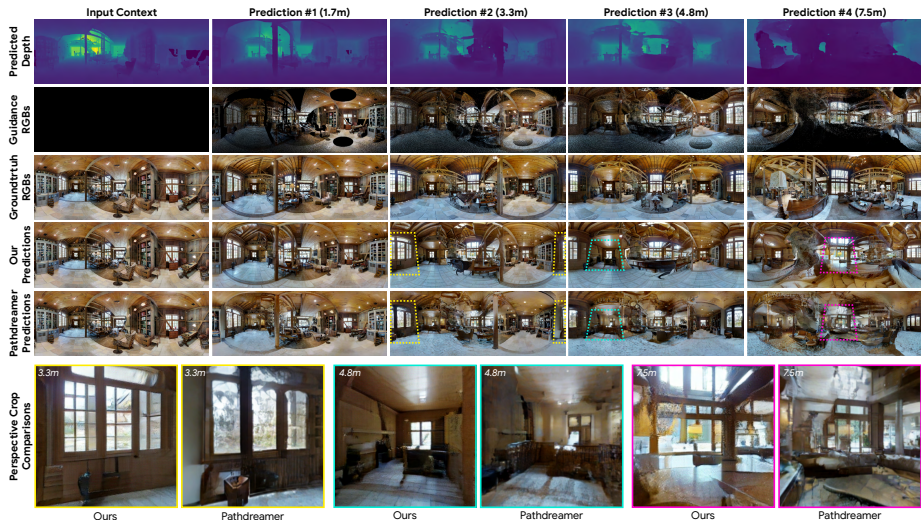
(c) At 4.0m, our model infills and completes the scene, imagining and generating a complete countertop for the kitchen.

Fig. 10: Randomly sampled examples of predicted sequences from the Val-Unseen R2R split of Matterport3D using one ground truth observation as context.



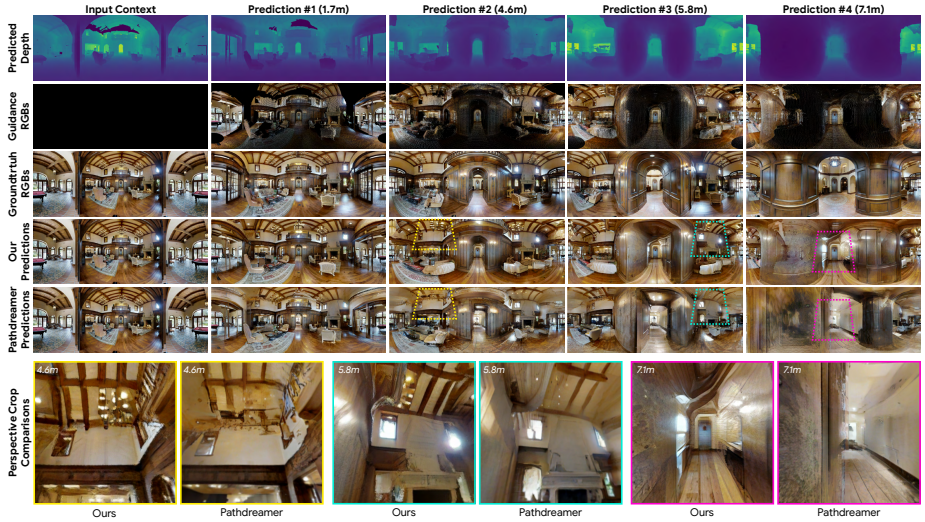


(a) Our model generates higher quality ceiling beams compared to Pathdreamer at 4.6m and 5.8m. Our model is also able to replicate a portion of the ceiling lights at 4.6m, which Pathdreamer is unable to do. Our generation results produce higher quality textures in general, such as the hardwood floors and carpet at 4.6m.

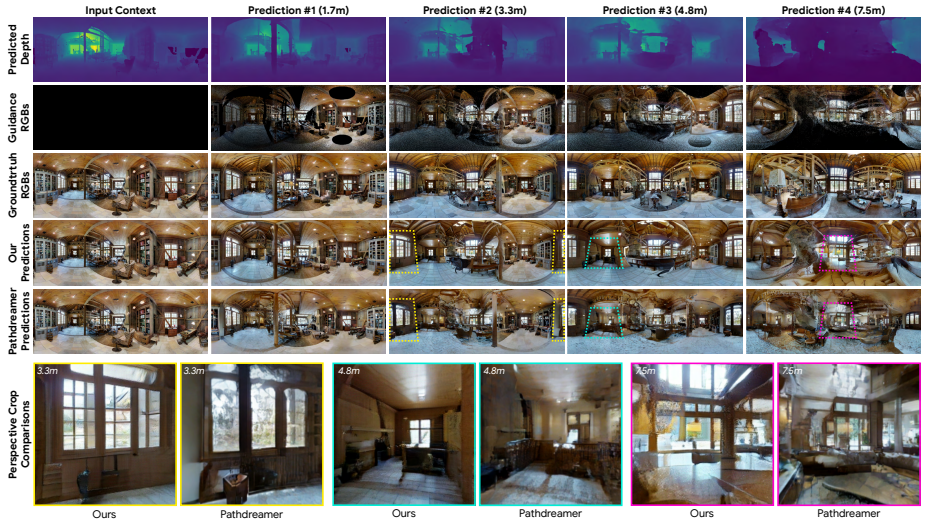


(b) Our model produces clearer windows, and is able to replicate the checkbox pattern of the window frame at 3.3m. At 4.8m, our model is able to generate a more coherent scene of a table and a window, compared to Pathdreamer which generates blurry and indistinctive outputs. Our model is also capable of generating objects more distinctly compared to Pathdreamer, such as the lamp at 7.5m.

Fig. 11: Selected examples comparing our model to Pathdreamer. One RGB-D pano is provided as context, and a sequence of novel viewpoints are generated.



(a) Our model generates higher quality ceiling beams compared to Pathdreamer at 4.6m and 5.8m. Our model is also able to replicate a portion of the ceiling lights at 4.6m, which Pathdreamer is unable to do. Our generation results produce higher quality textures in general, such as the hardwood floors and carpet at 4.6m.



(b) Our model produces clearer windows, and is able to replicate the checkbox pattern of the window frame at 3.3m. At 4.8m, our model is able to generate a more coherent scene of a table and a window, compared to Pathdreamer which generates blurry and indistinctive outputs. Our model is also capable of generating objects more distinctly compared to Pathdreamer, such as the lamp at 7.5m.

Fig. 12: Selected examples comparing our model to Pathdreamer. One RGB-D pano is provided as context, and a sequence of novel viewpoints are generated.



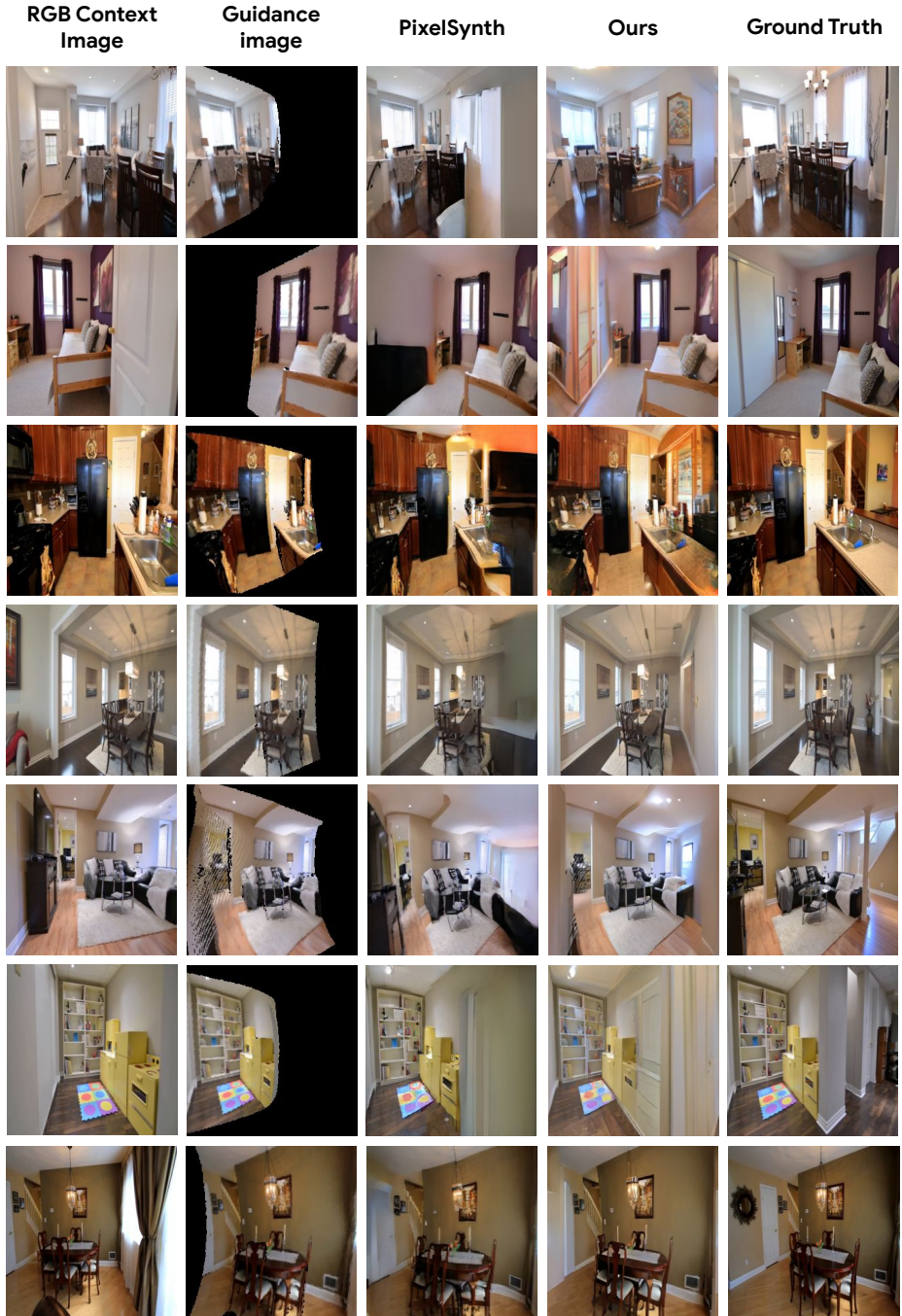


Fig. 13: Cherry picked examples of predicted sequences from the evaluation split of RealEstate10K using one ground truth observation as context.

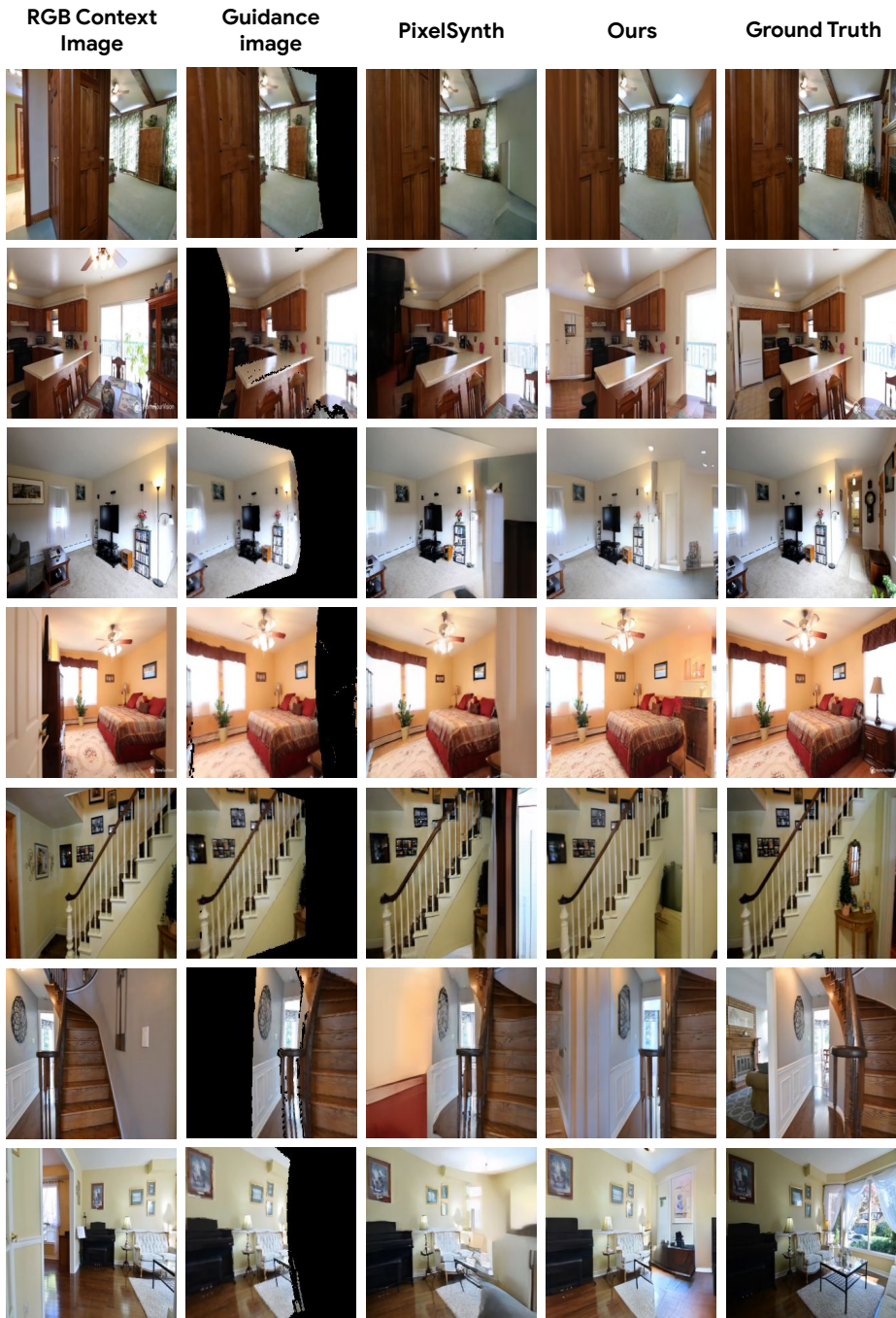


Fig. 14: Random sampled examples of predicted sequences from the evaluation split of RealEstate10K using one ground truth observation as context.